Figure S1. **a** and **b** show that the intraclast breccia and packstone (ICB) between stromatolite heads (STROM) may be dominated by either gray and beige spalled flakes of stromatolite and bacterial-mat stabilized mud (ICB$_{STROM}$) or red bioclasts (ICB$_{BCLST}$). **c** shows that Trezona Fm bioclast packstones with identical preservation as those found in situ with Trezona Fm stromatolite reefs (Fig. 2) also are found as clasts (ICB$_{BCLST}$ CLAST) in the overlying Elatina Fm diamictite (e.g., UTM WGS84: 0285315, 6632791) as far as 65 km from the nearest Trezona Fm stromatolite reef outcrop (Note that in **c**, the diamictite (DIAMICTITE MATRIX) is partly obscured by lichen). This relationship suggests that the composition and appearance of the distinctive red bioclasts was achieved during growth of the organism or early diagenesis, prior to glacial erosion.
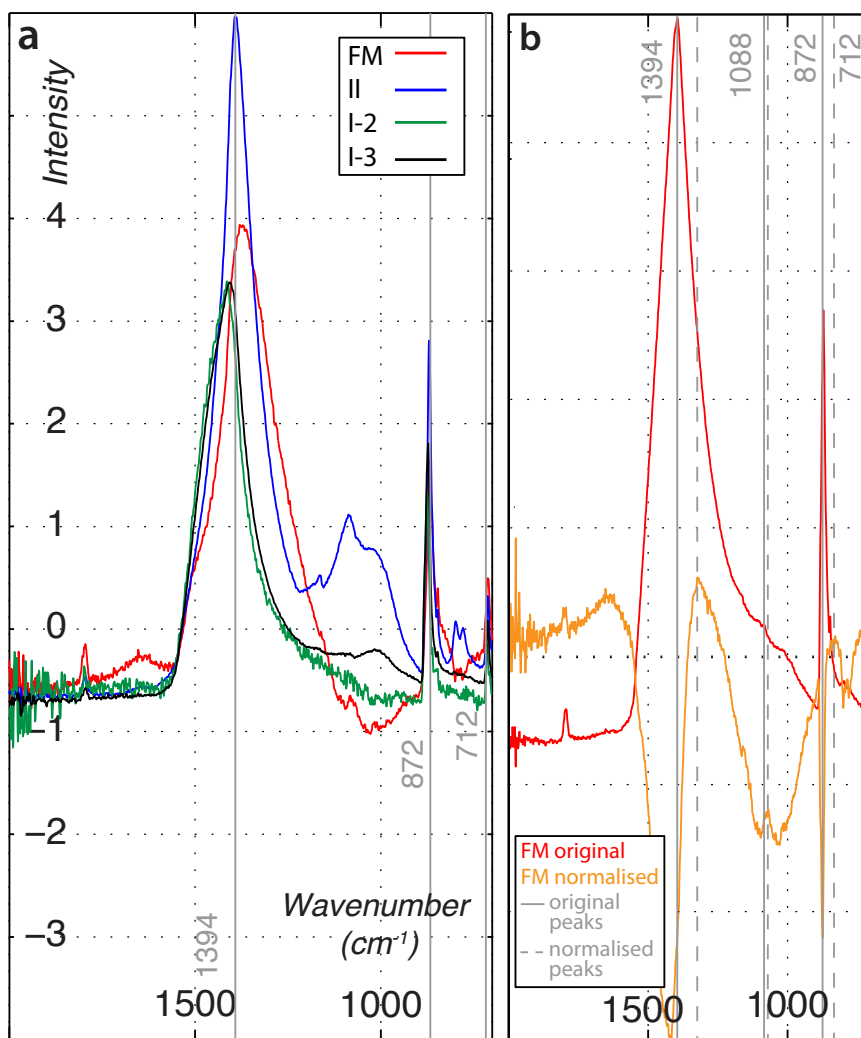
Figure S2. **a**, Attenuated total reflectance Fourier transform infrared (ATR-FTIR) spectra for four limestone samples within the Trezona Fm, South Australia. The spectra were obtained on a Bruker IFS66v/S (Billerica, MA) instrument using a narrow band mercury cadmium telluride (MCT) detector at Princeton University. Each curve represents the spectrum for powder derived from a red bioclast, minus the spectrum from powder prepared from the adjacent calcite matrix. The resultant spectra show three peaks indicative of calcium carbonate, annotated with solid grey vertical lines. **b**, All resultant spectra were normalized to progressively remove the peaks associated with calcium carbonate in the matrix and to isolate contributions from elements unique to the bioclasts. The close-up of the 1394 and 872 calcium carbonate peaks for sample 'FM' (red) shift (orange) to lower wavenumber peaks (dashed lines), consistent with bioclast enrichment in $MnCO_3$ or $FeCO_3$. H_2O_2 reactions with powdered samples (red product) and E-SEM electron probe work (Fig. 2**p**) confirmed that Fe is found preferentially within the bioclasts, where no Mn was detected with these methods.
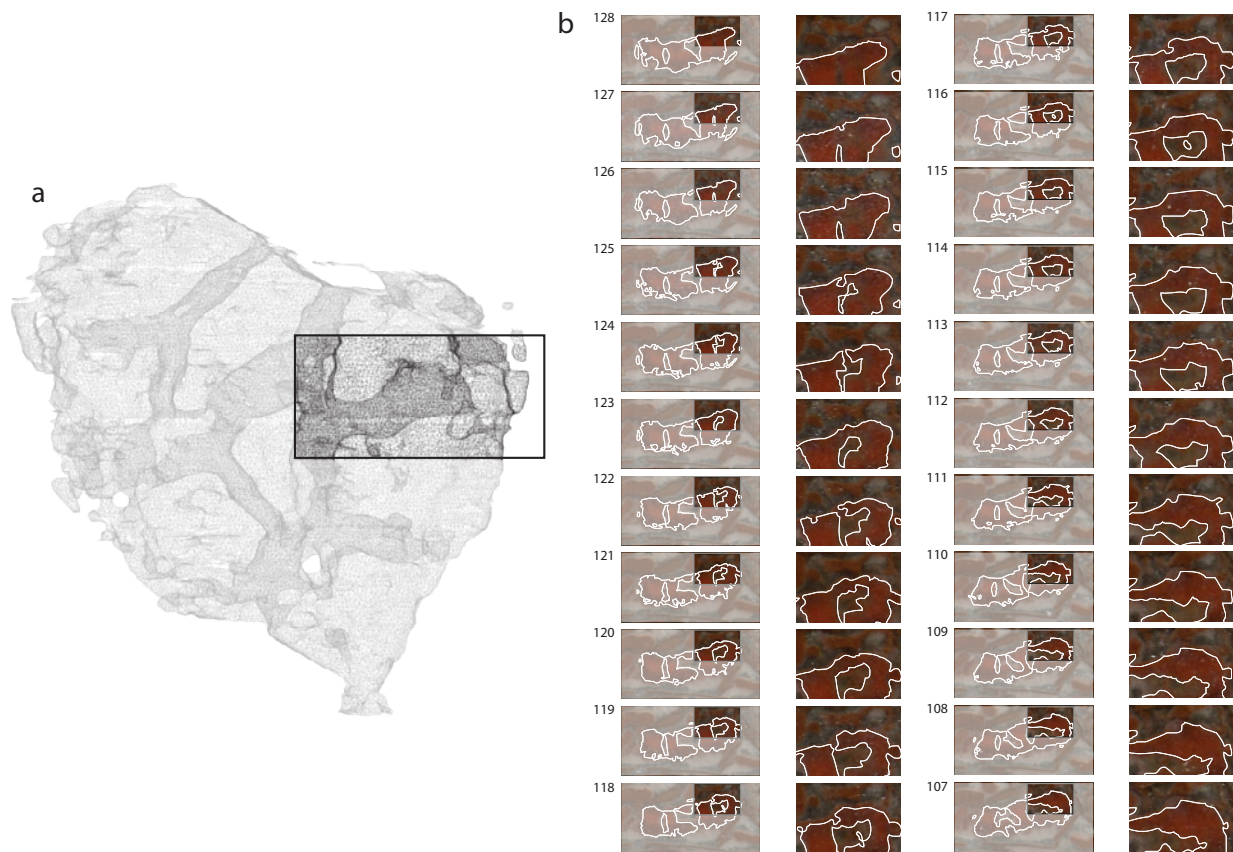
Figure S3. **a**,Triangular mesh of the fossil presented in Figure. 3**b,c**. The only interior canal in any of the modeled objects that appears to be a dead-end (i.e., a canal not open to the exterior through a circular aperture) is outlined with a back box. **b**, Frames 107-128 are the original digital scans taken after each 50.8 μm grind. The object used to reconstruct the fossil in **a** is autotraced in white in each frame. The region of the putative dead-end (black box in **a**) is enlarged adjacent to each full frame in **b** to allow for close scrutiny of the canal opening. This interrogation of the digital model and the original imagery suggests that even this canal opens to the exterior of the object (see the opening in frames 122-125).
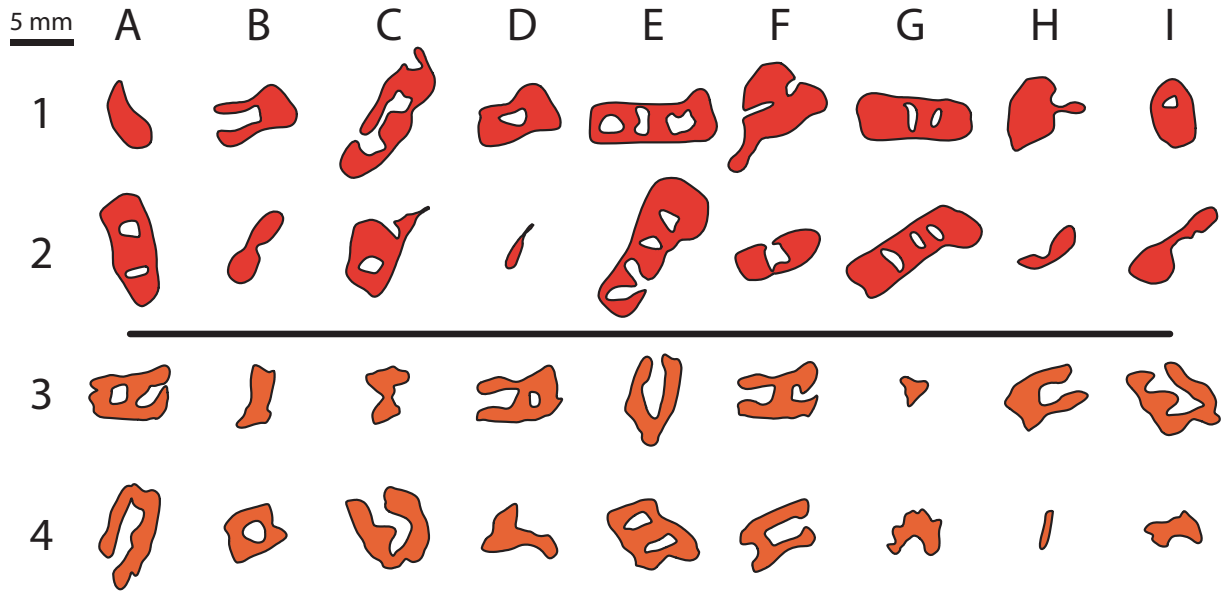
Figure S4. For each 3D model presented in Figure 3, we extract 624 2D sections (78 equally spaced sections taken through the entire specimen at eight different angles (i.e., every 45°)) and compare them to the common 2D sections apparent in outcrop (Fig. 2**d-g**). Rows 1 and 2 (red) correspond to Figure 3**c**, while Rows 3 and 4 (orange) correspond to Figure 3**f**. Anvils (3F, 4F), wishbones (1B, 3E, 3I), horsehoes (1B, 3H, 4A, 4C, 4F), rings (1I, 4B), tri-stars (3G), and perforated slabs (1E, 1G, 2A, 2E, 2G, 3A, 3D, 4E) are similar in scale and morphology between outcrop photos and the slices through the quantitative 3D models.

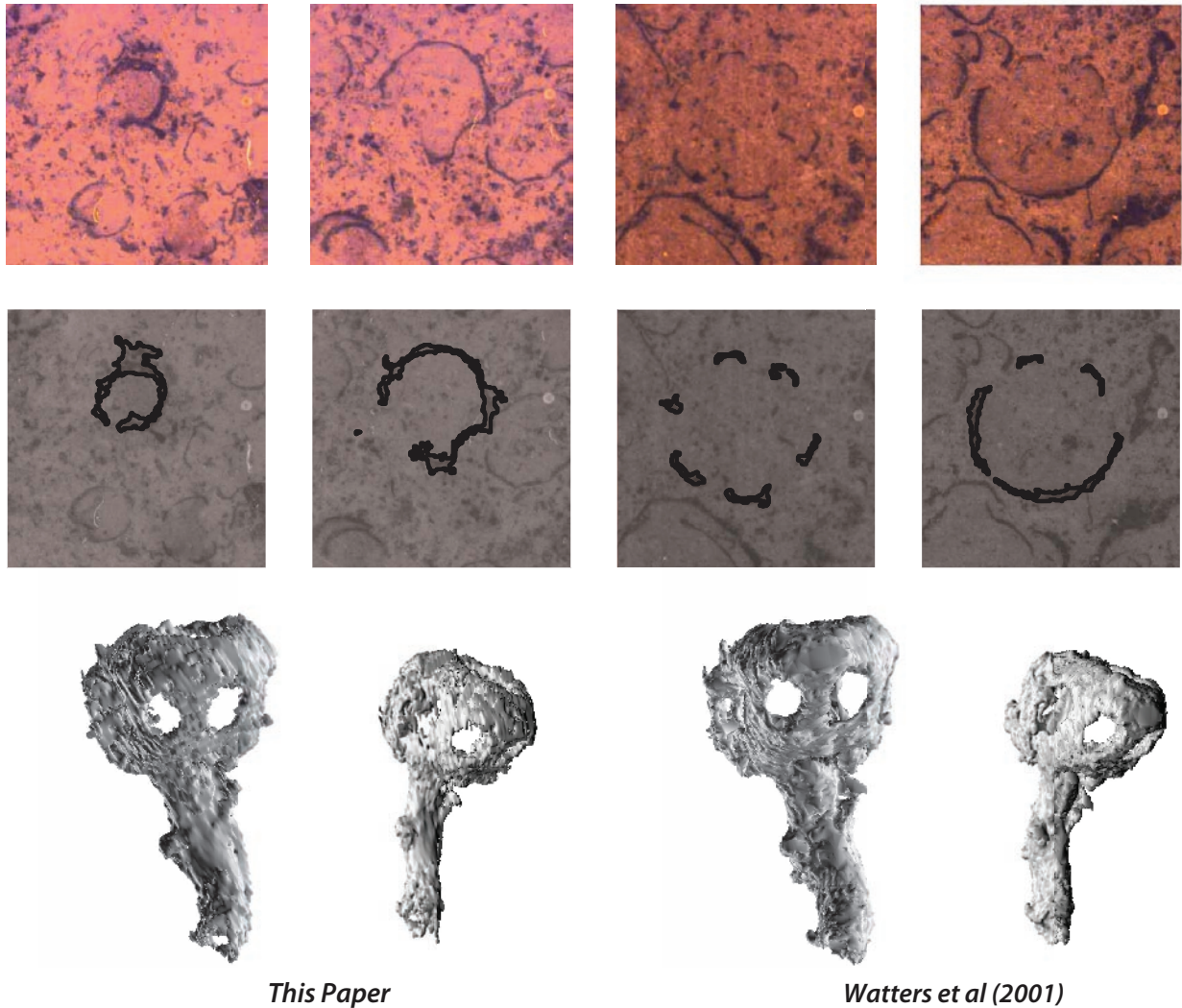*This Paper*   *Watters et al (2001)*

Figure S5. We take the original *Namacalathus* packstone imagery of Watters et al. (2001) (top row) and use the new software routine to perform autotraces (middle row). The new software generates 3D fossil reconstructions (bottom left) that are qualitatively and quantitatively similar to those of Watters et al. (2001) (bottom right).